LLNL-JRNL-2001751

Lawrence Livermore National Laboratory

Exploiting intersubband plasmons in vertically aligned carbon nanotubes for near-infrared electrochromic windows

A Abelson, A Hiszpanski

September 2025

ACS Nano Letters

Disclaimer

This work performed under the auspices of the U.S. Department of Energy by Lawrence Livermore National Laboratory under Contract DE-AC52-07NA27344.

Exploiting intersubband plasmons in vertically aligned carbon nanotubes for near-infrared electrochromic windows

Alex Abelson[1], Philip M. Jean-Remy[1], Tom Nakotte[2], Paul E. Munger[3], Steven F. Buchsbaum[1], Sei Jin Park[4], Anna M. Hiszpanski[2*]

[1] *Materials Engineering Division, Lawrence Livermore National Laboratory, Livermore, CA 94550, USA*
[2] *Materials Science Division, Lawrence Livermore National Laboratory, Livermore, CA 94550, USA*
[3] *Global Security Computing Applications Division, Lawrence Livermore National Laboratory, Livermore, CA 94550, USA*
[4] *Biosciences and Biotechnology Division, Lawrence Livermore National Laboratory, Livermore, CA 94550, USA*

*Corresponding Author: hiszpanski2@llnl.gov

Peer-reviewed Publication: https://pubs.acs.org/doi/10.1021/acs.nanolett.5c00059

Please cite as: *Nano Lett.* 2025, 25, 31, 11762-11767

Abstract

Optically transparent materials with switchable near-infrared (NIR) transmissivity are of significant interest for energy-saving smart window technologies. To this end, we demonstrate that semitransparent films of vertically aligned carbon nanotubes (CNTs) incorporated into electrochemically gated devices exhibit NIR transmittance changes up to 47% and bistable optical states that are appealing for low-power, large-area operation. The tunable NIR electrochromic response is driven by a doping-induced intersubband plasmon (ISBP) absorption, an optical feature in CNTs that is selective to light polarized perpendicular to the CNT axis. Vertically aligned CNT films (as opposed to more conventional planar CNT mats) thus allow us to isolate and study the ISBP resonance changes with applied voltage, electrode material, and film thickness

Results and Discussion

While electrochromic materials that modulate visible light have received significant attention for display[1] and dynamic tinting applications,[2,3] near-infrared (NIR) electrochromic materials are far less developed.[4–7] Interest in such NIR electrochromic materials is in part motivated by their potential to aide in thermal regulation of buildings by controllably filtering NIR solar radiation.[8] Among materials that exhibit NIR electrochromism,[9] carbon nanotube (CNT) thin films are promising candidates by virtue of their chemical stability, highly accessible surfaces, and infrared

absorption features with intensities that can be effectively modulated through double-layer (electrochemical) gating.[10–12] Indeed, CNTs have been integrated into electrochromic or optoelectric modulation devices in the form of random-packed CNT thin films that, upon gating (or doping), exhibit changes in their near-, mid-, far-infrared, or terahertz absorption.[13–18]

One limitation of these prior examples is that, by virtue of their random-packing, the CNT orientation is not fixed with respect to the polarization of incident light. CNTs exhibit optical responses that depend on polarization: undoped CNTs absorb visible/NIR light polarized parallel to their long axis, while they are nearly transparent to light that is polarized perpendicularly.[19] Upon doping, the interband absorption correlated with parallel polarization bleaches and a new absorption feature in the NIR correlated with perpendicular polarization appears.[20] This NIR absorption feature is attributed to intersubband plasmons (ISBP), which are optically driven charge density oscillations confined by the CNT diameter.[21–23]

In this paper we fabricate electrochromic devices using single-walled, vertically aligned carbon nanotubes (VACNTs) – thin films of CNTs grown perpendicular to the substrate – and evaluate their spectral and temporal responses to electrochemical gating.[24] As a result of their vertical alignment, these films exhibit >30% transparency across the visible portion of the spectrum and ISBP transmittance in the NIR that varies up to 47% with electrochemical gating, making them particularly appealing for smart-window applications. Furthermore, these devices exhibit optical states that persist for >100 s in open-circuit, a prerequisite for low-power operation. Finally, we perform numerical modeling of the devices to understand how the Fermi level of the CNTs relates to their spectral response, providing both a deeper understanding of ISBP photophysics and a series of potential design modifications to boost the optical modulation depth in pursuit of viable NIR smart-windows.

VACNTs grown by chemical vapor deposition (CVD) were directly integrated into electrochemical devices featuring three electrodes: VACNT working and counter electrodes and a metallic quasi-reference electrode (Figure 1a and 1b; see Methods). First, for each electrode, either Ti/Pt or TiN traces were lithographically patterned onto sapphire substrates. Next, CNT catalyst stacks containing alumina, Fe, and Mo were evaporated to partially overlap the metal traces and ultimately define the VACNT portions of the device (Figure S1).

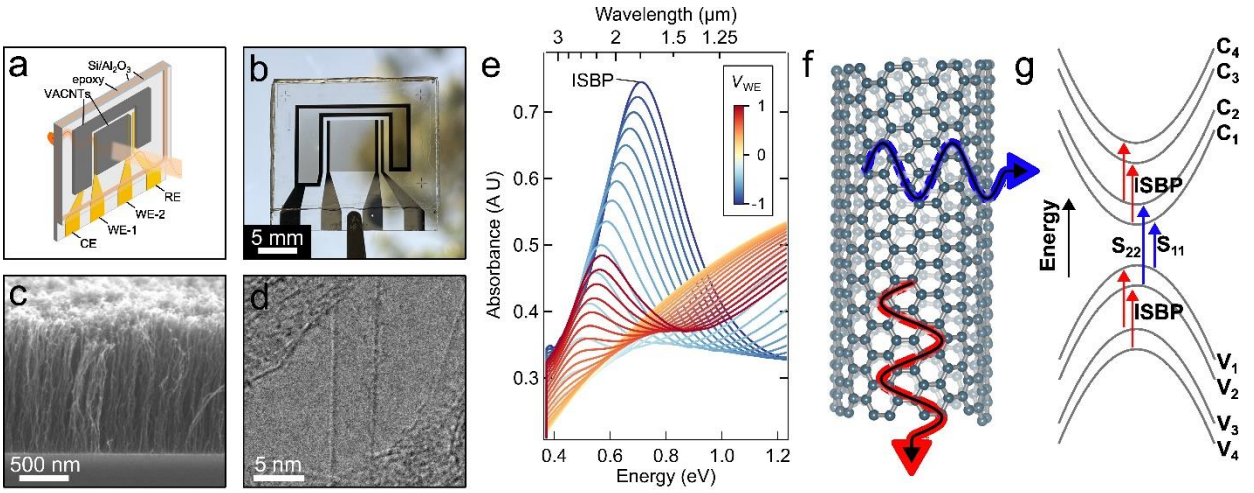

Figure 1. Intersubband plasmon absorption in vertically aligned carbon nanotube electrochromic devices. a) Schematic and (b) image of a completed device. **c)** Cross-sectional SEM image of an as-made VACNT forest on Si (see Methods) cleaved along the center of the optically active region of the device. **d)** Representative TEM image of a CNT. **e)** Infrared absorption spectra of a VACNT film for V_{WE} between −1 and 1 V relative to the Pt quasi-reference electrode. The broad, prominent peak is assigned to intersubband plasmon absorption. Spectra were baseline corrected to eliminate peaks from the ionic liquid (see Figure S7 for raw spectra). **f)** Interaction of a CNT with light propagating along two orthogonal directions. **g)** Corresponding optical transitions between conduction (C_n) and valence band (V_n) states of a semiconducting CNT. Light polarized parallel to the CNT axis (blue) excites interband transitions whereas light polarized perpendicular (light propagating with normal incidence to the VACNTs) excites only ISBP transitions.

Consistent with prior VACNT synthesis from our laboratory, we grew >98% single-wall purity VACNTs with a diameter range of 2.6 ± 0.7 nm (Figure 1c,d) and a high degree of graphitization (see Figure S2).[25,26] Grazing-incidence X-ray scattering measurements and cross-sectional images show that the CNTs are highly oriented, with an out-of-plane orientation distribution of only ± 6° (Figure S3). Electrical characterization of ~ 1 μm thick VACNT films yielded sheet resistances of ~ 20 kΩ·sq^{-1} , with a total contact resistance (for Ti/Pt contacts) of less than 0.5 kΩ (see Figures S4 and S5). To form the completed electrochromic devices, VACNT-patterned substrates were adhered with epoxy to bare sapphire substrates and then vacuum infiltrated with the ionic liquid 1- ethyl-3-methylimidazolium bis(trifluoromethylsulfonyl)imide (EMIM TFSI). Completed devices with 0.8 μm thick VACNT films are colorless and exhibit >50% transmittance across the visible spectrum (Figure S6), appropriate for residential and commercial windows.

As shown in Figure 1e, the undoped VACNTs (working electrode voltage, V_{WE}, = 0 V) exhibit a gently sloping NIR absorption profile that increases in intensity at higher photon energies. Upon electrochemical gating of the VACNT device, we observe pronounced and reversible ISBP

absorption in the NIR. Decreasing V_{WE} below −0.3 V (electron doping, blue traces in Figure 1e) or above 0.4 V (hole doping, red traces in Figure 1e) leads to ISBP absorption. The ISBP peak is first visible at a photon energy of 0.5 eV and, with larger potentials, both intensifies and blue shifts up to 0.7 eV. For this sample, the largest change in optical transmittance (≈ 24%) occurs at a photon energy of 0.68 eV and is fully reversible with cycling. The intensity and energy of ISBP absorption is reproducible in CNT films with thicknesses between 0.8 and 6.2 μm (Figure S8). This increase in absorption with doping contrasts with previous results from random-packed CNT films, which exhibited strong interband absorption in the undoped state, followed by relatively weaker ISBP absorption in the doped state.[22] The difference can be attributed to the vertical alignment present in our films: normally incident light is polarized perpendicular to the CNT axis and therefore does not excite interband optical transitions that lie in the NIR. Instead, normally incident light strongly excites the ISBP mode (see Figure 1f,g).[20–22] For electrochromic window applications, we next focused on evaluating and improving key performance metrics, including absorption strength in the NIR, switching speeds, and optical bistability. The absorption strength of the ISBP feature increases with applied electrochemical bias, and so we explored the broadest possible electrochemical window. The results presented in Figure 1 were limited to ± 1 V by the experimentally determined electrochemical stability window. Significant oxidative currents were observed above 1.2 V, attributable to the irreversible oxidation or dissolution of the Pt electrodes (Figure S9).[27]

To expand the electrochemical stability window, we looked at alternative contact materials compatible with the high VACNT growth temperature (800 °C), identifying TiN as a viable substitute for the Pt traces. For ease of fabrication, we also changed the quasi-reference electrode to TiN. The sheet resistance of these traces was significantly higher than that of the Ti/Pt, but larger electrochemical potentials were attainable without immediately oxidizing/dissolving the contacts (see Figure S10). Figure 2 shows the spectroelectrochemical response of a TiN electrode device measured from V_{WE} = −2 to 2 V, revealing a maximal change in transmittance of 47% at 0.83 eV, nearly twice that of the Pt contact device. A direct comparison of the optical transmittance for devices with Pt and TiN traces is shown in Figure 2b. Interestingly, the TiN-contacted film shows tunability across the entire spectral window from 0.6 to 1.2 eV (∼1-2 μm), further highlighting the potential utility of these materials as dynamic NIR electrochromic windows. While TiN contacts enabled greater NIR modulation, this improvement came at the cost of significantly slower

switching speeds (10s of seconds) because of TiN's high sheet resistance. Future efforts to improve the TiN conductivity should enable retention of the improved NIR modulation while also capturing the fast switching speeds of Ti/Pt devices, as discussed below.

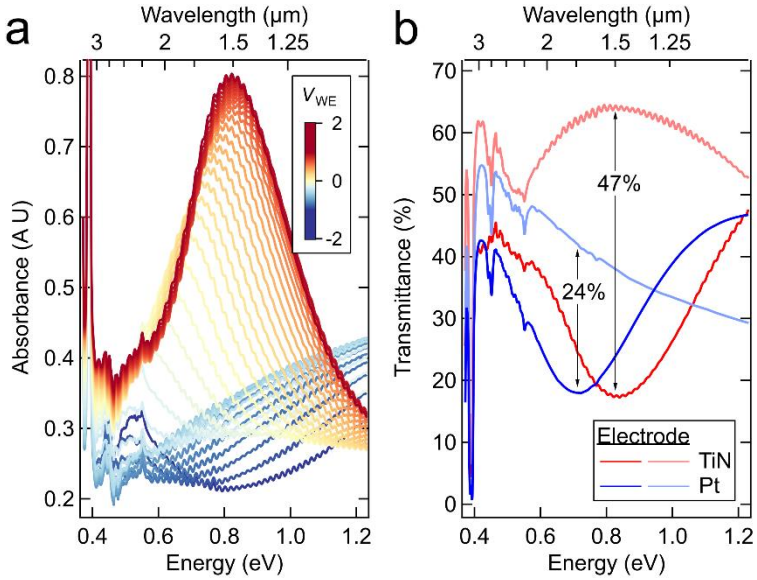

Figure 2. Impact of electrode composition on electrochromic response of VACNTs. a) Infrared extinction spectra of a VACNT film for V_{WE} between −2 and 2 V relative to the TiN quasi-reference electrode. V_{WE} was held for 120 s prior to each optical measurement. **b)** Transmission spectra of gated VACNT devices with TiN (red) and Pt (blue) traces. For TiN electrodes, the most and least transmissive states were achieved at +2 and −2 V vs TiN, respectively. For Pt electrodes, the most and least transmissive states were achieved at −0.3 and −1 V vs Pt, respectively.

Optical switching speeds, state volatility, and cycling stability are additional important performance metrics for electrochromic window applications. Figure 3a shows the VACNT transmittance at a photon energy of 0.76 eV upon cycling a Ti/ Pt-contact device between 0 and 1 V. The t_{90} times (the time it takes to reach 90% of the steady-state transmittance) are in the range of one to ten seconds. The temporal response is dominated by a large device capacitance (~500 μF) and relatively high resistance of the CNT films (~1 − 100 kΩ), rather than ion conductance limitations. Due to their higher areal capacitance and sheet resistance, VACNT electrochromic devices show slower switching speeds than comparable planar CNT mats (t_{90} ~ 1 ms).[14] Figure 3a also shows that the switching speeds are asymmetric ($t_{90,on}$ ~ 6 s and $t_{90,off}$ ~ 1 s), which we attribute to the significant difference in CNT film resistance between the undoped and doped states. Figure 3b shows the time-dependent optical response during potentiostatic control and upon switching to an open-circuit configuration. Interestingly, the device shows very slow discharge rates, retaining

after 100 s ~ 90% of the optical transmittance change, in agreement with other large-area (high capacitance) ionic liquid-based[16] and iongel[28] CNT capacitors.

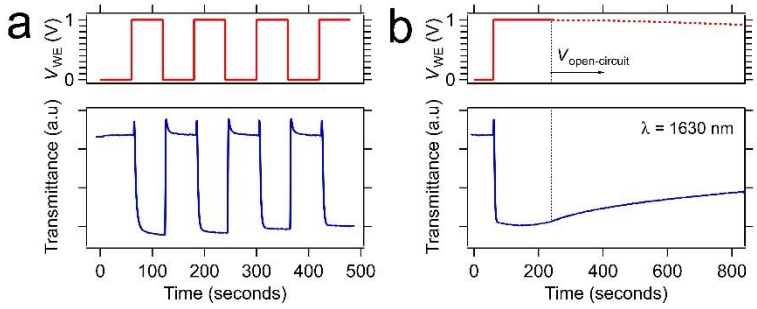

Figure 3. Transient optical and electronic response of CNT electrochromic devices. a) Transient optical response at a wavelength of 1630 nm upon switching of V_{WE} between 0 and 1 V. The characteristic on and off times are 6 and 1 s, respectively. Small spikes apparent at the beginning and end of each 0 V step are due to the device transiting the open-circuit potential (where the transmittance is maximized), which was slightly above 0 V. **b)** Electronic charging and optical state volatility upon switching the device to an open-circuit condition. The devices measured here have Ti/Pt traces.

Owing to the chemical stability of both the ionic liquid and CNTs, the devices show promising short-term and long-term stability. We subjected a Ti/Pt-contact device to 50 potential cycles over the course of 3 h and observed no degradation in performance (Figure S11). Furthermore, benchtop aging over more than 600 days yields no apparent loss in optical modulation efficiency (Figure S11).

To better understand how our VACNT devices operate, we examined the optical response as a function of the Fermi level. Recent numerical studies have predicted the ISBP energy (E_p) as a function of the CNT Fermi level (E_F), but this relationship was challenging to map in experiments utilizing horizontally laying CNTs due to weak ISBP absorption and the presence of convoluting interband absorption.[21–23] Figure 4a shows the ISBP peak energy and through-plane CNT conductance of a Ti/Pt contact device as a function of the applied electrochemical potential. As expected, the devices exhibit ambipolar transport characteristics, meaning we can inject electrons and holes into the CNTs, and that ISBP absorption occurs for both carrier types. Furthermore, E_p increases with the conductance G, which is expected based on the plasmonic character of the ISBP feature.

Following previous examples,[29–32] we calculated the Fermi level as a function of the applied electrochemical potential by modeling the CNT/IL interface as a simple series arrangement of the CNT quantum capacitance (C_Q) and electric double layer capacitance (C_{dl}), explicitly

incorporating the Kornyshev model of ionic liquid capacitance,[33,34] CNT density of states, CNT diameter distribution, thermal broadening, nanoscale curvature of the CNTs, and accounting for the presence of both metallic and semiconducting CNTs (see Supplementary Discussion 1).[35] Figure 4b shows the calculated double layer and quantum capacitance as a function of Fermi level for CNTs with the experimentally derived diameter distribution of 2.6 ± 0.7 nm, along with the corresponding electronic density of states for semiconducting and metallic CNTs (Figure 4c).[36]

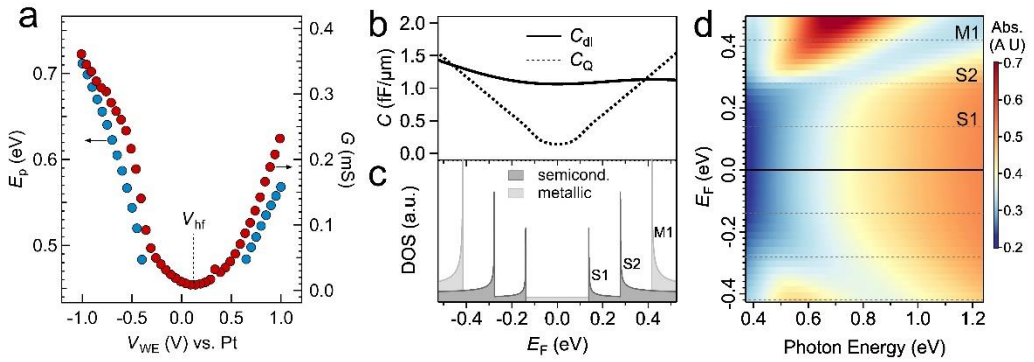

Figure 4. Impact of doping level and polarity on intersubband plasmon absorption. a) ISBP peak energy (E_p) and CNT conductance (G) versus the electrochemical potential relative to the Pt reference electrode. V_{hf} is the half-filling potential and corresponds to the Fermi level being at mid gap. b) Capacitance of CNTs (C_Q) and the double layer (C_{dl}) for d_{CNT} = 2.6 ± 0.7 nm CNTs as a function of the Fermi level (E_F). c) Calculated density of states for 2.6 nm semiconducting and metallic CNTs following Ref 30. No thermal- or size-broadening are included in this graphic for clarity (but are included in the full calculations). d) Experimental 2D VACNT absorption spectra as a function of the calculated Fermi energies. Annotated on the plot are horizontal lines indicating the first and second semiconducting van Hove singularities, as well as the first metallic van Hove singularity. This plot was generated from experimental data presented in Figure 1e.

The results of these calculations were combined with the spectroelectrochemical data presented in Figure 1 to produce the 2D plot shown in Figure 4d. In both electron and hole doping regimes, ISBP absorption is not discernible when E_F lies within the first set of van Hove singularities (vHs) (S_1 = ± 0.14 eV). Shifting E_F beyond the first vHs leads to the initial stages of weak ISBP absorption; however, not until E_F is into the second vHs does ISBP absorption dominate the NIR response. The strength and energy of the ISBP peak further increase as the Fermi level is shifted into the first metallic vHs (M_1) and out toward the edges of the measurement range. Our observation that ISBP absorption begins upon filling the second vHs agrees with previous calculations.[21] When the Fermi level is near or beyond the second vHs there is an optical bleach at photon energies between 0.8 and 1.2 eV that runs parallel to the ISBP peak trajectory (see Figure

4d). At these photon energies we are likely observing a bleach of S_{22} and M_{11} optical transitions (~0.56 and ~ 0.83 eV) in CNTs which are slightly misaligned from the substrate normal.[20]

A direct comparison between the performance of devices constructed from VACNTs and CNT mats is challenging as additional factors beyond CNT geometry − such as the CNT diameters, CNT thicknesses, operating voltage range, and electrode materials − affect performance. Nonetheless, comparing the performance of our VACNT devices (d_{CNT} = 2.6 nm, thickness ~ 800 nm) to Moser et al.'s[14] devices prepared with single-wall CNT mats (d_{CNT} = 1.5 nm, thickness = 114 nm), the latter attain a higher maximal transmittance modulation in the NIR (69% versus 47% for VACNTs) but at a lower photon energy (0.69 eV versus 0.83 eV for VACNTs). To maximize thermal regulation without degrading visible transparency, electrochromic NIR windows should be transparent across the visible and maximize transmittance modulation just red of the visible portion of the spectrum (~ 700 nm or 1.8 eV). To this end, further efforts to improve VACNT-based NIR electrochromic windows should focus on blue-shifting the absorption maximum by using smaller diameter CNTs, improving the degree of vertical alignment, and identifying electrode materials that are both compatible with high-temperature CVD growths, resistant to electrochemical oxidation, and that exhibit low sheet resistance. Beyond their potential for NIR electrochromic windows, VACNT electrochromic devices are a powerful platform for studying the polarization-dependent photophysics of CNTs and have enabled us to study CNTs' ISBP in isolation, experimentally mapping the ISBP energy as a function of Fermi energy.

Supporting Information

Experimental methods, flow chart of device fabrication, CNT chemical and structural analysis, structural characterization of CNT alignment, electrical characterization of CNT-integrated devices, electron microscopy of the CNT/electrode interface, optical spectra of the CNT films, raw spectroelectrochemical data, spectra showing the impact of CNT film thickness on infrared opacity, cyclic voltammetry of devices and electrode materials, short- and long-term cycling data, and detailed calculations of the CNT and double layer capacitance.

Author Information

Corresponding Author

Anna M. Hiszpanski − *Materials Science Division, Lawrence Livermore National Laboratory, Livermore, California 94550, United States; orcid.org/0000-0002-2705-3263; Email: hiszpanski2@llnl.gov*

Authors

Alex Abelson − *Materials Engineering Division, Lawrence Livermore National Laboratory, Livermore, California 94550, United States*

Philip M. Jean-Remy − *Materials Engineering Division, Lawrence Livermore National Laboratory, Livermore, California 94550, United States*

Tom Nakotte − *Materials Science Division, Lawrence Livermore National Laboratory, Livermore, California 94550, United States*

Paul E. Munger − *Global Security Computing Applications Division, Lawrence Livermore National Laboratory, Livermore, California 94550, United States*

Steven F. Buchsbaum − *Materials Engineering Division, Lawrence Livermore National Laboratory, Livermore, California 94550, United States*

Sei Jin Park − *Biosciences and Biotechnology Division, Lawrence Livermore National Laboratory, Livermore, California 94550, United States*; orcid.org/0000-0001- 6877-1512

Author Contributions

AA designed, fabricated, measured, analyzed the CNT devices and wrote the manuscript. PMJR synthesized the CNTs and performed Raman, SAXS, and TEM image analysis. TN helped perform

(spectro)electrochemical measurements. PEM helped with double-layer capacitance modeling efforts. SB helped develop the device architecture. SJP advised on CNT synthesis and characterization and performed TEM. AMH initiated and directed the study. All authors provided input to the manuscript.

Acknowledgements

This work was performed under the auspices of the U.S. Department of Energy by Lawrence Livermore National Laboratory under Contract DE-AC52-07NA27344 and supported by LDRD 23-ERD-049. We thank Thomas Ferron for assistance with small-angle X-ray scattering experiments. Work at the Molecular Foundry was supported by the Office of Science, Office of Basic Energy Sciences, of the U.S. Department of Energy under Contract No. DE-AC02-05CH11231. LLNL-JRNL-2001751.

Table of Contents Figure

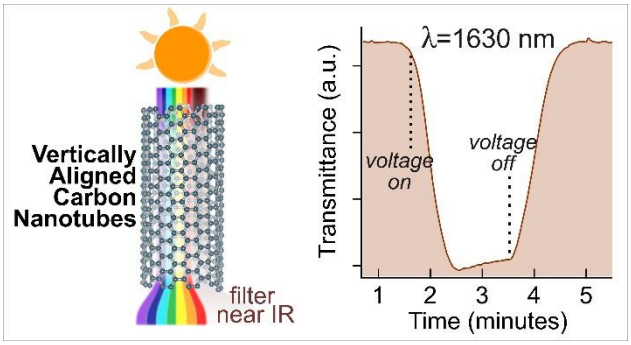

References

[1] Gu, C.; Jia, A.-B.; Zhang, Y.-M.; Zhang, S. X.-A. Emerging Electrochromic Materials and Devices for Future Displays. *Chemical Reviews* **2022**, *122* (18), 14679-14721. DOI: 10.1021/acs.chemrev.1c01055.

[2] Tällberg, R.; Jelle, B. P.; Loonen, R.; Gao, T.; Hamdy, M. Comparison of the energy saving potential of adaptive and controllable smart windows: A state-of-the-art review and simulation studies of thermochromic, photochromic and electrochromic technologies. *Solar Energy Materials and Solar Cells* **2019**, *200*, 109828. DOI: https://doi.org/10.1016/j.solmat.2019.02.041.

[3] Wang, Y.; Runnerstrom, E. L.; Milliron, D. J. Switchable Materials for Smart Windows. *Annual Review of Chemical and Biomolecular Engineering* **2016**, *7* (Volume 7, 2016), 283-304. DOI: https://doi.org/10.1146/annurev-chembioeng-080615-034647.

[4] Gong, H.; Li, W.; Fu, G.; Zhang, Q.; Liu, J.; Jin, Y.; Wang, H. Recent progress and advances in electrochromic devices exhibiting infrared modulation. *Journal of Materials Chemistry A* **2022**, *10* (12), 6269-6290, 10.1039/D1TA10970G. DOI: 10.1039/D1TA10970G.

[5] Wang, Z.; Gong, W.; Wang, X.; Chen, Z.; Chen, X.; Chen, J.; Sun, H.; Song, G.; Cong, S.; Geng, F.; et al. Remarkable Near-Infrared Electrochromism in Tungsten Oxide Driven by Interlayer Water-Induced Battery-to-Pseudocapacitor Transition. *ACS Applied Materials & Interfaces* **2020**, *12* (30), 33917-33925. DOI: 10.1021/acsami.0c08270.

[6] Llordés, A.; Garcia, G.; Gazquez, J.; Milliron, D. J. Tunable near-infrared and visible-light transmittance in nanocrystal-in-glass composites. *Nature* **2013**, *500* (7462), 323-326. DOI: 10.1038/nature12398.

[7] Barile, C. J.; Slotcavage, D. J.; McGehee, M. D. Polymer–Nanoparticle Electrochromic Materials that Selectively Modulate Visible and Near-Infrared Light. *Chemistry of Materials* **2016**, *28* (5), 1439-1445. DOI: 10.1021/acs.chemmater.5b04811.

[8] DeForest, N.; Shehabi, A.; O'Donnell, J.; Garcia, G.; Greenblatt, J.; Lee, E. S.; Selkowitz, S.; Milliron, D. J. United States energy and CO2 savings potential from deployment of near-infrared electrochromic window glazings. *Building and Environment* **2015**, *89*, 107-117. DOI: https://doi.org/10.1016/j.buildenv.2015.02.021.

[9] Garcia, G.; Buonsanti, R.; Runnerstrom, E. L.; Mendelsberg, R. J.; Llordes, A.; Anders, A.; Richardson, T. J.; Milliron, D. J. Dynamically Modulating the Surface Plasmon Resonance of Doped Semiconductor Nanocrystals. *Nano Letters* **2011**, *11* (10), 4415-4420. DOI: 10.1021/nl202597n.

[10] Wu, Z.; Chen, Z.; Du, X.; Logan, J. M.; Sippel, J.; Nikolou, M.; Kamaras, K.; Reynolds, J. R.; Tanner, D. B.; Hebard, A. F.; et al. Transparent, Conductive Carbon Nanotube Films. Science 2004, 305 (5688), 1273-1276. DOI: doi:10.1126/science.1101243.

[11] Kavan, L.; Rapta, P.; Dunsch, L.; Bronikowski, M. J.; Willis, P.; Smalley, R. E. Electrochemical Tuning of Electronic Structure of Single-Walled Carbon Nanotubes: In-situ Raman and Vis-NIR Study. The Journal of Physical Chemistry B 2001, 105 (44), 10764-10771. DOI: 10.1021/jp011709a.

[12] Itkis, M. E.; Niyogi, S.; Meng, M. E.; Hamon, M. A.; Hu, H.; Haddon, R. C. Spectroscopic Study of the Fermi Level Electronic Structure of Single-Walled Carbon Nanotubes. Nano Letters 2002, 2 (2), 155-159. DOI: 10.1021/nl0156639.

[13] Wang, F.; Itkis, M. E.; Haddon, R. C. Enhanced Electromodulation of Infrared Transmittance in Semitransparent Films of Large Diameter Semiconducting Single-Walled Carbon Nanotubes. *Nano Letters* **2010**, *10* (3), 937-942. DOI: 10.1021/nl9038423.

[14] Moser, M. L.; Li, G.; Chen, M.; Bekyarova, E.; Itkis, M. E.; Haddon, R. C. Fast Electrochromic Device Based on Single-Walled Carbon Nanotube Thin Films. *Nano Letters* **2016**, *16* (9), 5386-5393. DOI: 10.1021/acs.nanolett.6b01564.

[15] Gagnon, P.; Lapointe, F.; Desjardins, P.; Martel, R. Double-walled carbon nanotube film as the active electrode in an electro-optical modulator for the mid-infrared and terahertz regions. *Journal of Applied Physics* **2020**, *128* (23), 233103. DOI: 10.1063/5.0031466.

[16] Sun, Y.; Chang, H.; Hu, J.; Wang, Y.; Weng, Y.; Zhang, C.; Niu, S.; Cao, L.; Chen, Z.; Guo, N.; et al. Large-Scale Multifunctional Carbon Nanotube Thin Film as Effective Mid-Infrared Radiation Modulator with Long-Term Stability. *Advanced Optical Materials* **2021**, *9* (3), 2001216, https://doi.org/10.1002/adom.202001216. DOI: https://doi.org/10.1002/adom.202001216.

[17] Lynch, P. J.; Tripathi, M.; Amorim Graf, A.; Ogilvie, S. P.; Large, M. J.; Salvage, J.; Dalton, A. B. Mid-Infrared Electrochromics Enabled by Intraband Modulation in Carbon Nanotube Networks. *ACS Applied Materials & Interfaces* **2023**, *15* (8), 11225-11233. DOI: 10.1021/acsami.2c19758.

[18] Arkook, B.; Chen, M. Dynamic Performance of Hybrid Infrared Modulator Based on Single-Walled Carbon Nanotubes and Ionic Liquid Enabling Fast Response. *Advanced Photonics Research* **2024**, *5* (2), 2300210. DOI: https://doi.org/10.1002/adpr.202300210.

[19] Murakami, Y.; Einarsson, E.; Edamura, T.; Maruyama, S. Polarization Dependence of the Optical Absorption of Single-Walled Carbon Nanotubes. *Physical Review Letters* **2005**, *94* (8), 087402. DOI: 10.1103/PhysRevLett.94.087402.

[20] Yanagi, K.; Okada, R.; Ichinose, Y.; Yomogida, Y.; Katsutani, F.; Gao, W.; Kono, J. Intersubband plasmons in the quantum limit in gated and aligned carbon nanotubes. *Nature Communications* **2018**, *9* (1), 1121. DOI: 10.1038/s41467-018-03381-y.

[21] Satco, D.; Nugraha, A. R. T.; Ukhtary, M. S.; Kopylova, D.; Nasibulin, A. G.; Saito, R. Intersubband plasmon excitations in doped carbon nanotubes. *Physical Review B* **2019**, *99* (7), 075403. DOI: 10.1103/PhysRevB.99.075403.

[22] Satco, D.; Kopylova, D. S.; Fedorov, F. S.; Kallio, T.; Saito, R.; Nasibulin, A. G. Intersubband Plasmon Observation in Electrochemically Gated Carbon Nanotube Films. *ACS Applied Electronic Materials* **2020**, *2* (1), 195-203. DOI: 10.1021/acsaelm.9b00695.

[23] Wang, F. T.; Yang, D. H.; Li, L. H.; Liu, Y. M.; Wei, X. J.; Zhou, W. Y.; Kataura, H.; Liu, H. P.; Xie, S. S. Electronic Type and Diameter Dependence of the Intersubband Plasmons of Single-Wall Carbon Nanotubes. *Adv. Funct. Mater.* **2022**, *32* (11), 8, Article. DOI: 10.1002/adfm.202107489.

[24] Ren, Z. F.; Huang, Z. P.; Xu, J. W.; Wang, J. H.; Bush, P.; Siegal, M. P.; Provencio, P. N. Synthesis of Large Arrays of Well-Aligned Carbon Nanotubes on Glass. *Science* **1998**, *282* (5391), 1105-1107.

[25] Meshot, E. R.; Park, S. J.; Buchsbaum, S. F.; Jue, M. L.; Kuykendall, T. R.; Schaible, E.; Bayu Aji, L. B.; Kucheyev, S. O.; Wu, K. J. J.; Fornasiero, F. High-yield growth kinetics and spatial mapping of single-

walled carbon nanotube forests at wafer scale. *Carbon* **2020**, *159*, 236-246. DOI: https://doi.org/10.1016/j.carbon.2019.12.023.

[26] Dresselhaus, M. S.; Dresselhaus, G.; Saito, R.; Jorio, A. Raman spectroscopy of carbon nanotubes. *Physics Reports* **2005**, *409* (2), 47-99. DOI: https://doi.org/10.1016/j.physrep.2004.10.006.

[27] Bengio, D.; Mendes, E.; Pellet-Rostaing, S.; Moisy, P. Electrochemical behavior of platinum and gold electrodes in the aprotic ionic liquid N,N-Trimethylbutylammonium Bis(trifluoromethanesulfonyl)imide. *Journal of Electroanalytical Chemistry* **2018**, *823*, 445-454. DOI: https://doi.org/10.1016/j.jelechem.2018.06.034.

[28] Berger, F. J.; Higgins, T. M.; Rother, M.; Graf, A.; Zakharko, Y.; Allard, S.; Matthiesen, M.; Gotthardt, J. M.; Scherf, U.; Zaumseil, J. From Broadband to Electrochromic Notch Filters with Printed Monochiral Carbon Nanotubes. *ACS Applied Materials & Interfaces* **2018**, *10* (13), 11135-11142.

[29] Li, J.; Pham, P. H. Q.; Zhou, W.; Pham, T. D.; Burke, P. J. Carbon-Nanotube–Electrolyte Interface: Quantum and Electric Double Layer Capacitance. *ACS Nano* **2018**, *12* (10), 9763-9774. DOI: 10.1021/acsnano.8b01427.

[30] Liang, J.; Akinwande, D.; Wong, H. S. P. Carrier density and quantum capacitance for semiconducting carbon nanotubes. *Journal of Applied Physics* **2008**, *104* (6), 064515. DOI: 10.1063/1.2986216.

[31] Ilani, S.; Donev, L. A. K.; Kindermann, M.; McEuen, P. L. Measurement of the quantum capacitance of interacting electrons in carbon nanotubes. *Nature Physics* **2006**, *2* (10), 687-691. DOI: 10.1038/nphys412.

[32] Verkholyak, T.; Kuzmak, A.; Kornyshev, A. A.; Kondrat, S. Less Is More: Can Low Quantum Capacitance Boost Capacitive Energy Storage? *The Journal of Physical Chemistry Letters* **2022**, *13* (47), 10976-10980. DOI: 10.1021/acs.jpclett.2c02968.

[33] Klein, J. M.; Panichi, E.; Gurkan, B. Potential dependent capacitance of [EMIM][TFSI], [N1114][TFSI] and [PYR13][TFSI] ionic liquids on glassy carbon. *Physical Chemistry Chemical Physics* **2019**, *21* (7), 3712-3720. DOI: 10.1039/c8cp04631j.

[34] Jitvisate, M.; Seddon, J. R. T. Direct Measurement of the Differential Capacitance of Solvent-Free and Dilute Ionic Liquids. *The Journal of Physical Chemistry Letters* **2018**, *9* (1), 126-131. DOI: 10.1021/acs.jpclett.7b02946.

[35] Dresselhaus, G.; Dresselhaus, M. S.; Saito, R. *Physical Properties Of Carbon Nanotubes*; World Scientific Publishing Company, 1998.

[36] Mintmire, J. W.; White, C. T. Universal Density of States for Carbon Nanotubes. *Physical Review Letters* **1998**, *81* (12), 2506-2509. DOI: 10.1103/PhysRevLett.81.2506.

Supporting Information

for

Exploiting intersubband plasmons in vertically aligned carbon nanotubes for near-infrared electrochromic windows

Alex Abelson[1], Philip M. Jean-Remy[1], Tom Nakotte[2], Paul E. Munger[3], Steven F. Buchsbaum[1], Sei Jin Park[4], Anna M. Hiszpanski[2*]

[1] *Materials Engineering Division, Lawrence Livermore National Laboratory, Livermore, CA 94550, USA*
[2] *Materials Science Division, Lawrence Livermore National Laboratory, Livermore, CA 94550, USA*
[3] *Global Security Computing Applications Division, Lawrence Livermore National Laboratory, Livermore, CA 94550, USA*
[4] *Biosciences and Biotechnology Division, Lawrence Livermore National Laboratory, Livermore, CA 94550, USA*

*Corresponding Author: hiszpanski2@llnl.gov

Methods and Materials

Materials. All materials were used as received unless otherwise noted. 4" C-plane sapphire wafers were purchased from Silicon Valley Microelectronics, Inc. Silicon wafers used for SEM imaging were intrinsic Si with 200 nm of low-stress PECVD Si_xN purchased from Addison Engineering. Negative tone AZ nLOF 2035 and positive tone AZ 1518, and AZ 300 MIF developer were purchased from MicroChemicals. For metal contact deposition, Ti (99.995%), Pt (99.99%) Fe (99.95%) Mo (99.95%) and Al_2O_3 (99.99%) were purchased from Kurt J. Lesker Company. 1-Ethyl-3-methylimidazolium bis(trifluoromethylsulfonyl)imide (EMIM TFSI; 99.5%) was purchased from IoLiTec Ionic Liquids Technologies. Spacer grade soda lime glass microspheres (23-26 μm) were purchased from Cospheric. Dymax 9037-F was purchased from Dymax. Norland UVS 91 was purchased from Norland. All solvents were cleanroom grade and purchased from CMC materials.

Device fabrication. Ti/Pt traces were first patterned onto Si or sapphire wafers. nLOF 2035 was spin coated at 3000 rpm onto a sapphire wafer, then soft-baked for 90 seconds at 110 °C. Next, the wafer was photopatterned by an MLA 150 maskless aligner (Heidelberg Instruments) with a 375 nm laser at a dose of 200 mJ cm^{-2}. The wafer was baked for 120 seconds at 110 °C, then developed by immersion in MIF 300 for 100 seconds. The wafer was rinsed with deionized water and blown dry. Prior to metallization, the wafer was O_2 plasma cleaned (Nordson March AP-300) for two

minutes in a downstream configuration at 150 W power. This plasma cleaning recipe was used throughout the device fabrication process. Ti (20 nm) and Pt (160 nm) were sequentially deposited by electron-beam evaporation at 1.2 Å s^{-1} and 2.0 Å s^{-1}, respectively. The base pressure of the evaporation system was between 2×10^{-7} and 1×10^{-6} Torr. 80 nm thick TiN electrodes were deposited by the Stratio Technology Nanofabrication Facility using a Perkin-Elmer 4400 sputter system operating at a pressure of 8 mTorr, a power of 200 W, and an Ar flow rate of 20 sccm at a deposition rate of 40 nm/hour. Lift-off was performed by soaking (> 1 hour) in acetone, followed by brief sonication (as needed). The wafers were briefly sonicated in deionized water and IPA, then rinsed with deionized water and blown dry in a spin-rinse-dry unit. Next, catalyst was deposited on the metallized wafer. First, the wafer was vapor primed with HMDS (Yield Engineering Systems) at 150 °C to promote photoresist adhesion. Next, AZ1518 was spin coated at 3000 rpm, then soft-baked for 90 seconds at 95 °C. The wafer was photopatterned by an MLA 150 maskless aligner with a 375 nm laser at a dose of 200 mJ cm^{-2}, then developed by immersion in MIF 300 for approximately one minute. The wafer was rinsed with deionized water and blown dry. Prior to catalyst deposition, the wafer was O_2 plasma cleaned. Al_2O_3, Fe, and/or Mo were deposited by electron beam evaporation in the same chamber as the CNT catalyst stack. Prior to evaporation, the chamber was evacuated overnight to a base pressure of 1.2×10^{-7} Torr. Lift-off was performed by soaking the wafer in acetone (> 3 hours), followed by brief sonication (as needed). The wafers were briefly sonicated in deionized water and IPA, then rinsed with deionized water and blown dry in a spin-rinse-dry unit. The wafers were then hand-diced, and briefly rinsed with IPA to remove wafer debris. Prior to CNT growth, the chips were O_2 plasma cleaned. Next, CNTs were grown using low-pressure chemical vapor deposition (CVD) within a cold-wall furnace (AIXTRON Black Magic Pro 4 in., Lawrence Berkeley National Laboratory) The CVD base pressure prior to growth runs was less than 10^{-2} Torr. Growth runs began with thermal annealing of the deposited catalyst layers before introducing the gaseous hydrocarbon precursor (C_2H_2). The growth recipe was as follows: ramp the temperature at 200 ^oC min^{-1} to 800 ^oC at 8.25 Torr in H_2/Ar = 700 sccm/200 sccm and maintain for 3.5 minutes before transitioning to a gas mixture of C_2H_2/H_2/Ar = 4/700/400 sccm at 8.25 Torr for the desired duration for the targeted thickness. 20 sccm of the total Ar flow during the growth step was routed through a bubbler containing H_2O to deliver 20 ppm_V of water vapor to the chamber.

Device Assembly. A slurry containing 3 wt% mixture of spacer beads in Dymax 9037F epoxy was deposited by syringe pump (Nordson Ultimus II) at the edges of the CNT/metal-patterned substrate with the aid of a home-built mechanical translation stage. The slurry was deposited around the full exterior, leaving a small gap for liquid infilling. A sapphire blank was then lowered onto the substrate and pressed into contact. The Dymax 9037F was UV cured for 30 minutes with a 365 nm UV exposure system (OAI 30) with a dose of 6.3 mW cm^{-2}, during which the CNTs were covered by a protective aluminum foil mask to prevent any potential UV degradation. The device stack was then heat cured on a hot plate at 150 °C for ~15 minutes. EMIM TFSI was infilled into the device stack using a custom vacuum infiltration system. The device was mounted vertically inside the vacuum chamber on a linear translation arm above a small pool of EMIM TFSI. The system was evacuated, and the device was lowered until the edge with the small epoxy gap was submerged. After complete infilling, the device was removed from the vacuum chamber and the edge was carefully painted with Norland UVS 91 epoxy, which was then UV exposed for 30 minutes (see above). Most of the IL and CNT film were covered with aluminum foil to limit any potential UV degradation/photolysis.

Characterization. Raman scattering spectroscopy was performed using an inVia Qontor confocal Raman microscope with an excitation wavelength of $\lambda = 633$ nm and an 8.2 mm working distance 50x objective lens (Leica Camera, Inc.). The system was calibrated with an internal Si wafer reference standard before each measurement. With a 1200 lines/mm grating, single-point spectra were obtained in the 100 – 1970 cm^{-1} range at 5% laser power. Each spectrum was baseline corrected and normalized to the G-band (~1594 cm^{-1}) prior to data analysis. Scanning electron microscopy was performed with a Thermo Fisher Verios 5 XHR. High resolution TEM (JEOL 2100-F) was used to quantify the CNT diameter distribution and wall purity. For each CNT forest, 100 – 200 datapoints were collected to synthesize a CNT diameter distribution histogram. Images were collected at 200 kV. To prepare the TEM samples, CNTs were harvested from the center and edge of forests and then dispersed in ethanol before finally being drop-casted onto TEM grids. Grazing incidence SAXS data were collected on a XEUSS 3.0 (Xenocs, Inc.). Measurements were collected using a Cu Kα source (8.05 keV), a PILATUS 300K Detector System (DECTRIS AG) with a pixel size of 0.172 mm × 0.172 mm, a sample-to-detector distance of 350 mm, and a sample tilt of 1°. SAXS data were reduced and analyzed using the MATLAB toolbox GIXGUI (Argonne National Laboratory).[1] An empty background image was subtracted from the collected scattering

patterns prior to analyses. UV-vis measurements were performed with a Perkin-Elmer Lambda 950 spectrophotometer with integrating sphere.

Electrochemical measurement. A potentiostat (Biologic SP-150) was used for electrochemical measurements. Electrical connection between the potentiostat and the device was facilitated by a custom-made jig with copper clips that contact the exposed Pt or TiN traces on the device. For three electrode measurements, the two working electrode leads were shorted. For four electrode measurements, two potentiostat channels were switched into the CE-to-ground mode and synchronized to one-another. The working electrode leads of each potentiostat channel were attached to the two working electrode leads on the device and a small dc offset was applied. In this configuration, the through-plane current is calculated as $\frac{1}{2}(I_1 - I_2)$ and the normal electrochemical current is calculated as $I_1 + I_2$.

Spectroelectrochemical measurement. The device was loaded into the sample position of a Bruker Vertex 70 Fourier transform infrared spectrometer (FTIR) and connected to the potentiostat. In a typical measurement, the device was biased for ~120 seconds prior to the start of the FTIR scan. The devices were measured in an automated fashion in either 50 mV or 100 mV steps, scanning from 0 to 1 V, then down to -1 V, then back to 0 V. For TiN electrode devices, the sweeps were extended to ± 2 V.

Time-dependent optical measurements. Spectroelectrochemical CNT devices were illuminated by a chopped (550 Hz) mono-chromated quartz tungsten halogen light source and the transmitted light was recorded on an InGaAs photodiode with a 17 ns rise time (Thor Labs Inc, FD05D). The photodiode signal was amplified using a transimpedance amplifier (SR570) outputting to a lock-in amplifier (SR830). The output of the lock-in amplifier was recorded on an oscilloscope (Tektronix MDO3104). The VACNT electrochromic device was concurrently biased using a potentiostat (Biologic SP-150).

Cyclic voltammetry of TiN and Ti/Pt electrodes. Thin films of TiN and Ti/Pt deposited on sapphire substrates were immersed in an electrochemical cell containing EMIM TFSI along with a 0.5 mm diameter Ag wire reference electrode and 3 mm diameter glassy carbon counter electrode (both purchased from CH Instruments Inc.). Cyclic voltammograms were measured at a sweep rate of 10 mV s^{-1}.

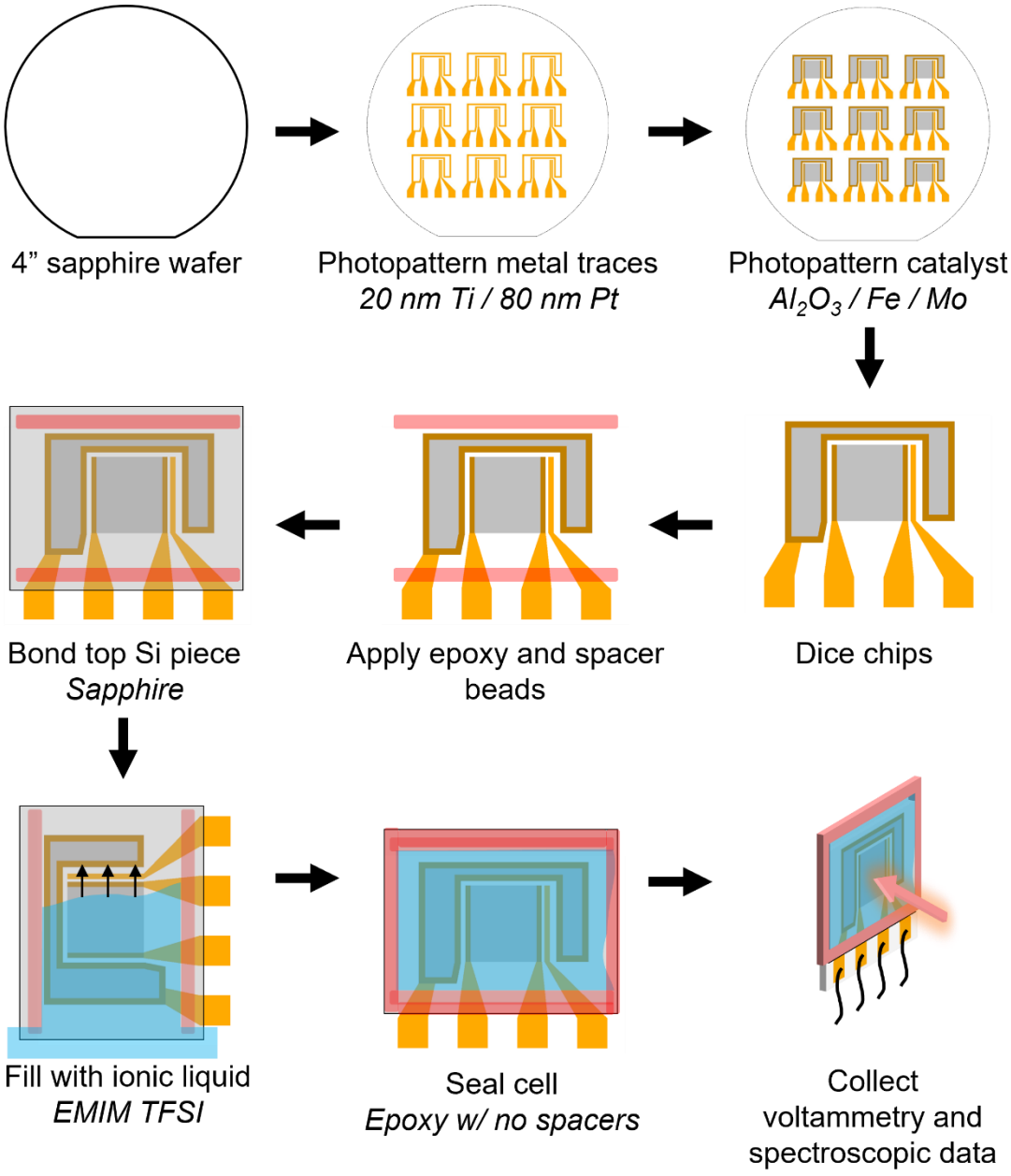

Figure S1. **Flow chart of VACNT spectroelectrochemical device fabrication.**

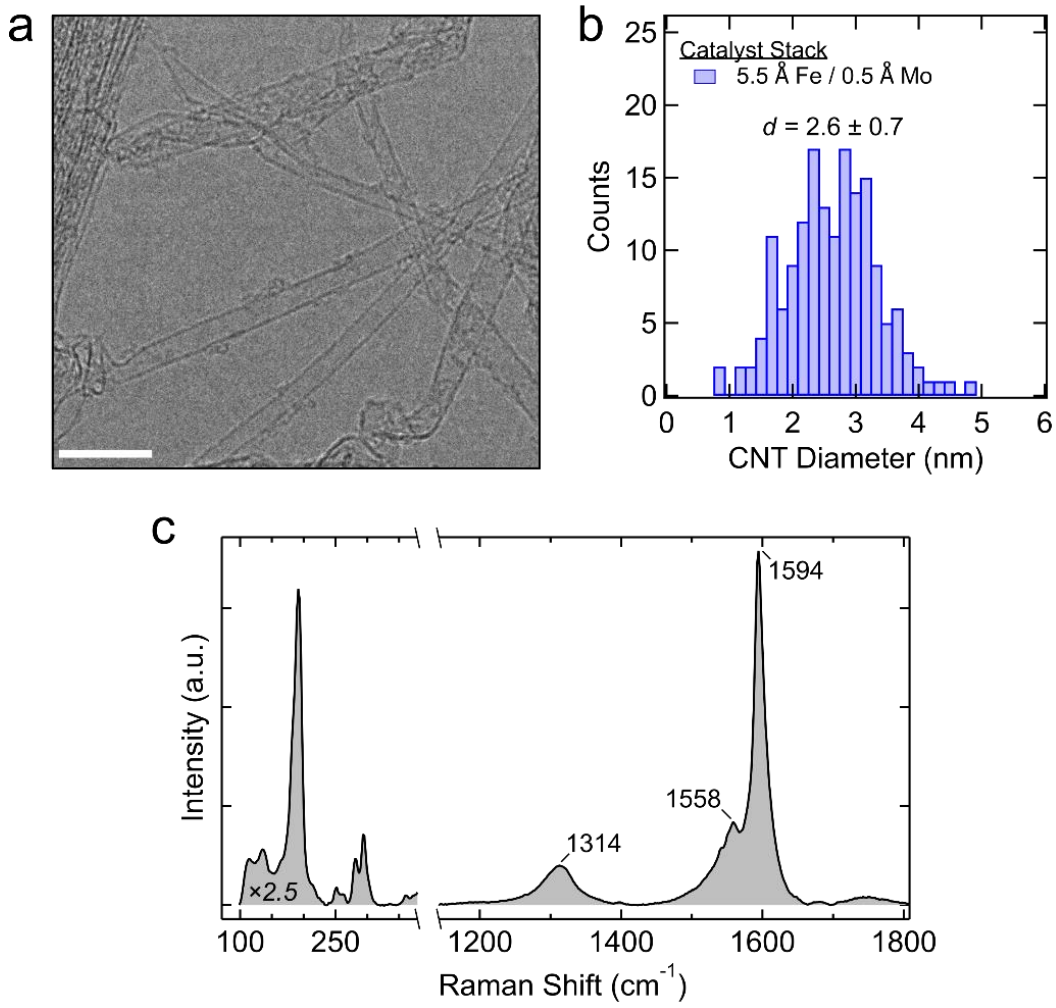

Figure S2. Analysis of carbon nanotubes used in this study. (a) Representative TEM image of CNTs grown on 5.5 Å Fe/0.5 Å Mo. For TEM analysis, CNTs were collected from ~50 µm films grown on sapphire substrates and suspended in a solvent prior to deposition on a TEM grid (see Methods). **b)** CNT diameter histogram extracted from numerous TEM images. Analysis of CNTs grown on 5.5 Å Fe/0.5 Å Mo catalyst yielded average diameter of 2.6 ± 0.7 nm (N = 164), where the reported error is the standard deviation of the data-set. **c)** Raman spectra of an as grown CNT forest on sapphire. Note the split axis. The spectrum on the left portion of the graph is multiplied by 2.5. The large G/D (peaks at 1594 and 1314 cm^{-1}, respectively) is indicative of a high degree of graphitization. Pronounced radial breathing modes in the low wavenumber range indicate a high proportion of single-wall CNTs, in agreement with TEM analysis.

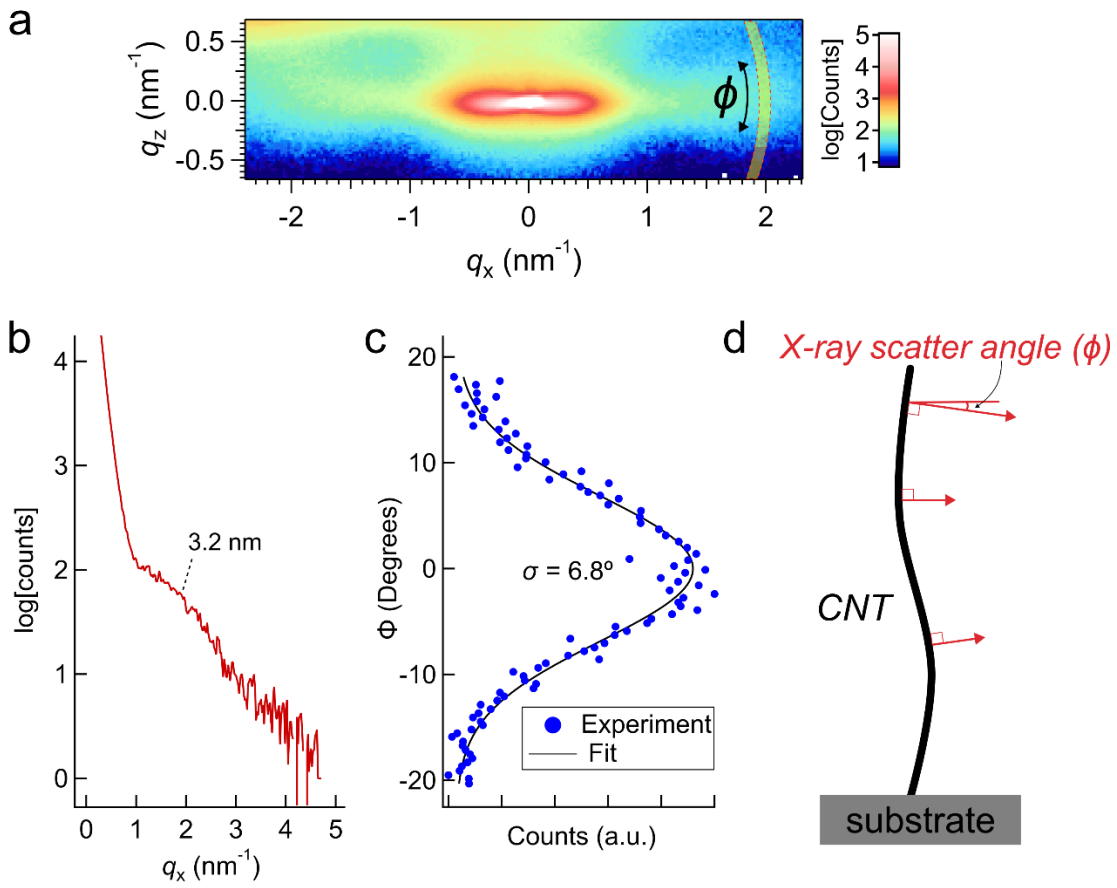

Figure S3. Quantitative analysis of CNT alignment using small-angle X-ray scattering (SAXS). a) SAXS pattern of a 50 µm VACNT film collected at a grazing incidence angle of 1° (see Methods). Rather than colleting the reflected signal, we collect the directly transmitted (refracted) portion of the beam. Indicated on the pattern is a the azimuthal (φ) cut used in panel (c). **b)** SAXS data vertically integrated along $q_z = \pm 0.5$ nm^{-1}. Annotated on the graph is the scattering vector corresponding to a characteristic scattering length of 3.2 nm. This slight hump in the SAXS profile corresponds to form factor scattering from the CNTs. We note that the SAXS-derived diameter is ~20% larger than the TEM results, in agreement with previous reports.[2] **c)** Azimuthal profile of the SAXS data to evaluate the degree of CNT misalignment. The scattering pattern was integrated radially between $q = 1.965 \pm 0.65$ nm^{-1}. The resulting azimuthal intensity line profile is well fit by a Gaussian distribution with a standard deviation of 6.8° (full width at half maximum of 16°). **d)** Schematic of how CNT tortuosity (misalignment from purely vertical) leads to broadening of the azimuthal intensity profile (panel c).

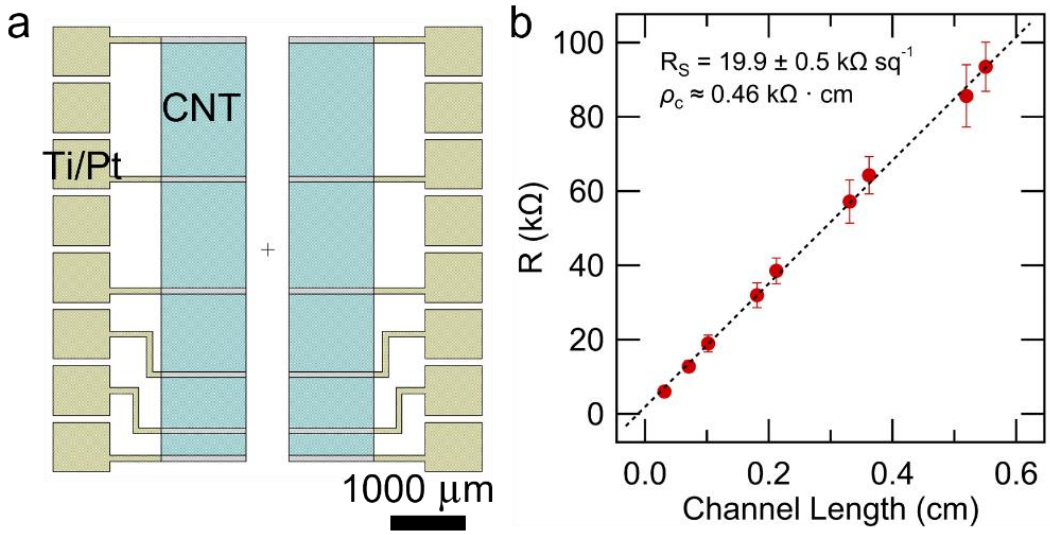

Figure S4. VACNT sheet and contact resistance. a) Schematic of the transmission line test device. Beige portions represent Ti/Pt traces and the aqua regions represent VACNTs. The scale bar is 1000 µm. **b)** Channel length-dependent resistance data. The slope of the fit (R/l) was multiplied by the channel width (0.12 cm) to arrive at the sheet resistance (R_S). The y-intercept is the contact resistance (R_C). The specific contact resistivity is the contact resistance multiplied by the total length of the metal-CNT contact (0.24 cm). Error bars represent the standard deviation calculated from six replicates. The film was approximately 1.2 µm thick and was in a dry state (no ionic liquid).

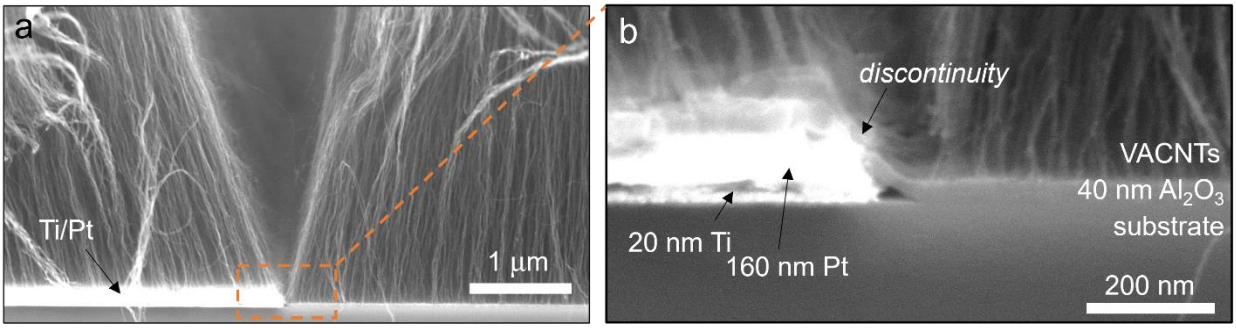

Figure S5. Analysis of the CNT/Pt interface. a) Cross-section SEM image of a VACNT film at the edge of a Ti/Pt trace. The scale bar is 1 µm. b) High-magnification image of the metal/CNT junction. Clearly visible are the Si substrate, 40 nm Al_2O_3 catalyst buffer layer, 20 nm Ti and 160 nm of Pt. Denoted in the image is the discontinuity in the Al_2O_3 layer at the edge of the metal trace. The scale bar is 200 nm.

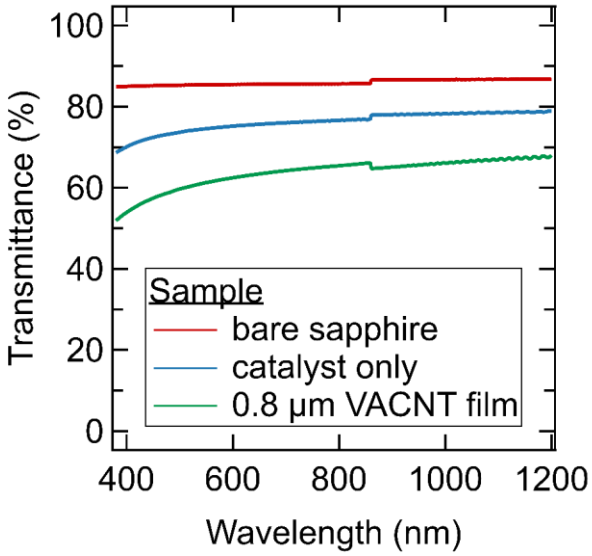

Figure S6. Optical transparency of a VACNT electrochromic device at steady-state. A single piece of bare sapphire admits > 80% of visible light. Constructing a full electrochromic device with patterned catalyst but no CNTs leads to 70-80% transparency across the visible and NIR. An un-gated 0.8 µm-thick VACNT film fully integrated into an electrochromic window (with ionic liquid) transmits > 50% of visible and > 60% NIR light.

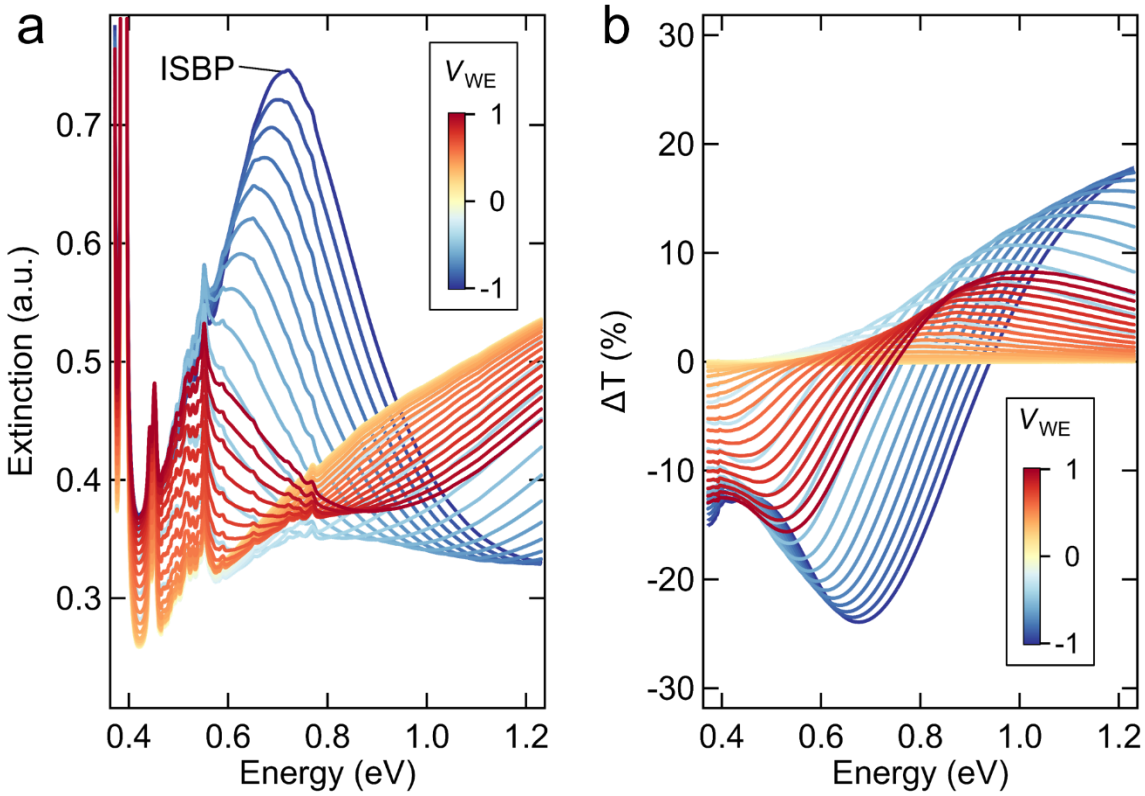

Figure S7. Supporting data for Figure 1. a) Raw spectra of the data shown in Figure 2a. Note the absorption features at low energy attributable to various vibrational modes of the ionic liquid. **b)** Transmission difference spectra of the device shown in Figure 2as defined as the change in transmittance at different working electrode potentials relative to $V_{WE} = 0$ V.

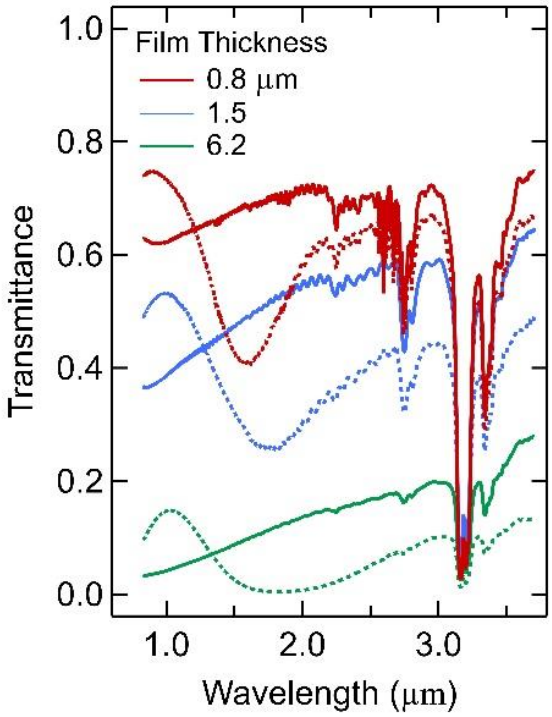

Figure S8. Impact of film thickness on ISBP absorption. The thickest films are nearly opaque in both doped (dashed lines) and undoped (solid lines) states, whereas the thinnest films (~0.8 μm) exhibit a high degree of NIR transparency. These devices were made with TiN electrodes, and therefore had a relatively small electrochemical stability window. In each case, the ISBP absorption feature is present around 1.7 μm.

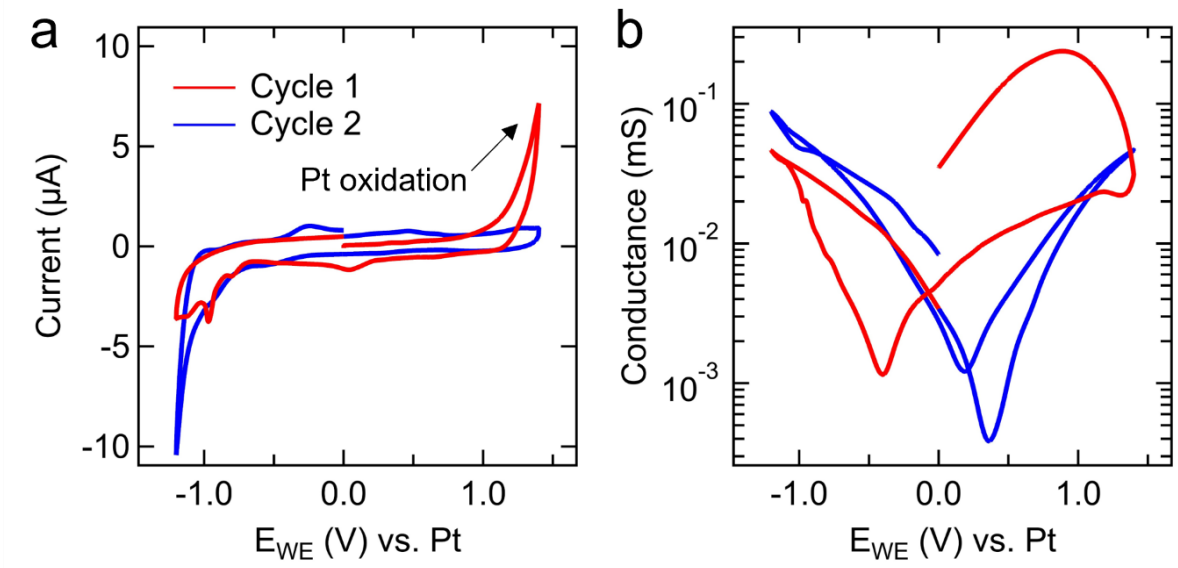

Figure S9. Oxidation of Ti/Pt electrodes and impact on CNT/Pt electrical contact. Initial potential sweeps of a 0.8 μm thick CNT device filled with EMIM TFSI. Upon the initial sweep we see a large oxidation current attributable to the irreversible oxidation of Pt. This large oxidation current is accompanied by a significant shift in V_{hf} from ~ -0.5 V on the initial sweep to ~ 0.4 V on the second. The prominent oxidation peak which we attribute to Pt oxidation is consistent with the findings of Moisy et al. who described a two-step process for the irreversible oxidation of Ti/Pt electrodes in EMIM TFSI.[3]

$$\text{Step 1: } Pt + H_2O \rightleftharpoons PtOH + H^+ + e^-$$

$$\text{Step 2: } PtOH \rightarrow PtO + H^+ + e^-$$

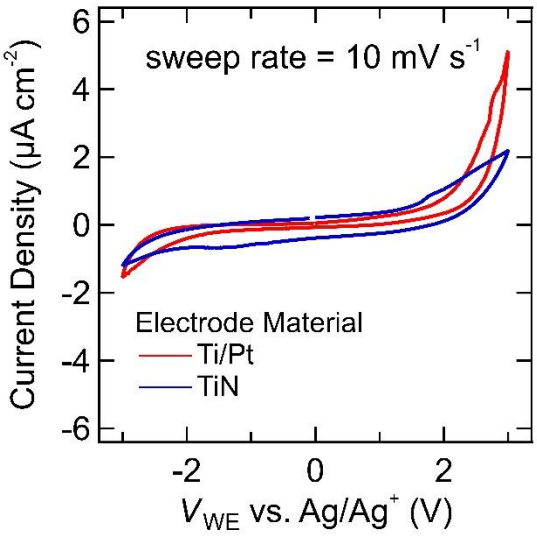

Figure S10. Cyclic voltammetry of TiN and Ti/Pt electrodes. Thin film electrodes deposited on sapphire were measured using three-electrode cyclic voltammetry with a Ag/Ag+ reference electrode. See Methods for additional details on the measurement conditions.

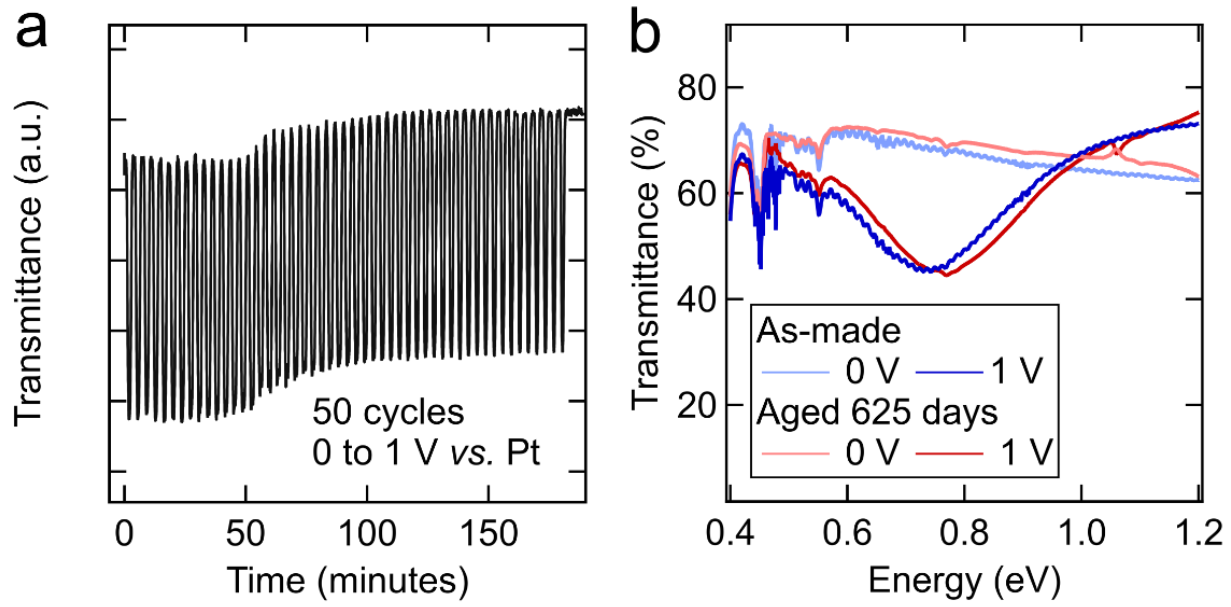

Figure S11. Short-term and long-term stability tests. a) Accelerated short-term testing of a VACNT device. The working electrode potential was cycled between 0 and 1 V for a total of 50 cycles. The shift in baseline is due to drift in the light source. The change in transmittance remains nearly constant throughout the test. **b)** Spectra of an as-made device and the same device measured 625 days after the initial measurement. The device was tested intermittently between these two dates and was otherwise stored on the lab bench.

Supplementary Discussion 1. Calculation of the chemical potential as a function of the working electrode potential.

All capacitance values are calculated and reported in units of capacitance/length (femto-Farads per micrometer).

Calculation of quantum capacitance.

To estimate the chemical potential μ of the CNTs as a function of the applied working electrode potential V_{WE} we follow the method of several previous reports.[4,5,6] The total potential drop across the device, ignoring *iR* drop, is:

$$V_{WE} - V_{hf} = V_{dl} + V_Q \quad [1]$$

where V_{dl} and V_Q are the potentials dropped across the double layer and the CNTs, respectively. V_{hf} represents the potential difference between the CNT half filling level and the Ti/Pt reference electrode and was identified experimentally as the working electrode potential at which the CNT conductance is minimized.

The total capacitance is modelled as a series arrangement of the double layer capacitance C_{dl} and quantum capacitance C_Q of the CNTs:

$$C_{tot}^{-1} = C_{dl}^{-1} + C_Q^{-1} \quad [2]$$

The capacitance terms depend on the potential drop across each respective layer and the diameter distribution of CNTs (which we quantify experimentally from TEM data).

First, we calculate the quantum capacitance of the CNTs (per unit length) from the definition of differential capacitance:

$$C_Q = -\frac{\partial q_L}{\partial \mu} \quad [3]$$

where q_L is the charge-per-unit-length. Given a density of states (DOS) as $\rho_L(E)$, q_L is calculated using:

$$q_L = e\int_{-\infty}^{\infty} f(E-\mu)\rho_L(E)dE \qquad [4]$$

where $f(E-\mu)$ is the Fermi-Dirac distribution function centered at chemical potential μ. The DOS for both metallic and semiconducting CNTs feature van Hove singularities at diameter-dependent energies ϵ_m that can be calculated according to the conditional expression:[7]

$$\epsilon_m = \frac{a_{cc}\gamma_0}{d}\begin{cases} 3m & \text{for metallic CNTs} \\ 3m+1 & \text{for semiconducting CNTs} \end{cases} \qquad [5]$$

where a = 0.144 nm is the carbon-carbon bond distance in graphene and γ_0 = 2.5 eV is the associated tight binding overlap energy. The DOS can be separated into terms which depend on energy and terms which do not. As such, we can write an expression g(E) which contains the energy dependence of the DOS:

$$g(E,\epsilon_m) = \begin{cases} \dfrac{|E|}{\sqrt{E^2-\epsilon_m^2}}, & |E| > |\epsilon_m| \\ 0, & |E| < |\epsilon_m| \end{cases} \qquad [6]$$

$$g(E,0) = 1$$

Combining [5] and [6], in addition to constant terms derived in Ref. 6, yields the DOS per carbon atom:[7]

$$\rho(E) = \frac{2\sqrt{3}a_{cc}}{\pi^2\gamma_0 d}\sum_{m=-i}^{i} g(E,\epsilon_m) \qquad [7]$$

We convert this into the DOS per unit length by multiplying by the CNT circumference and dividing by the area per carbon atom:

$$\rho_L(E) = \frac{2\sqrt{3}a_{cc}}{\pi\gamma_0 n_{cc}} \sum_{m=-4}^{4} g(E, \epsilon_m) \quad [8]$$

where $n_{cc} = 2.62 \cdot 10^{-20}$ m^2/atom is the area per carbon atom. With [8], we now have a functional form of $\rho_L(E)$, the density of states per length. Plugging [8] into [4] and taking the derivative with respect to μ gives us C_Q at a particular chemical potential and CNT diameter:

$$C_Q = e \sum_{m=-4}^{4} \int_{-\infty}^{\infty} dE f'(E-\mu)\rho_L(E) \quad [9]$$

where the integrand f' is the derivative of the Fermi-Dirac distribution with respect to μ:

$$f' = (4kT)^{-1} \operatorname{sech}^2\left(\frac{E-\mu}{2kT}\right) \quad [10]$$

Combining [8], [9], and [10], we can now evaluate the capacitance per unit length of the CNTs.

$$C_Q = \frac{2\sqrt{3}a_{cc}e}{4kT\pi\gamma_0 n_{cc}} \int_{-\infty}^{\infty} dE \operatorname{sech}^2\left(\frac{E-\mu}{2kT}\right) \sum_{m=-4}^{4} g(E, \epsilon_m) \quad [11]$$

We numerically evaluated the integral in [11] for $|E| > |\epsilon_m|$ to yield the capacitance per unit length. This quantity is single-valued for a particular chemical potential and CNT diameter. We next include a calculation which factors in the polydispersity of the CNTs by calculating the expectation value of C_Q over a normally-distributed population of CNT diameters:

$$\langle C_Q \rangle_d = \frac{1}{p} \sum C_Q(d)p(d) \quad [12]$$

where $p(d)$ is a normally-distributed probability density centered at d_{avg} with a standard deviation of σ. All reported quantum capacitance values account for polydispersity.

Finally, to account for the presence of both semiconducting and metallic CNTs in our samples, we take a weighted average of the capacitance values calculated using the selection rules in [5]. This is a reasonable thing to do because the CNTs are arranged in parallel with one another and their chemical potentials are nominally at equilibrium. We assume that 1/3 of the CNTs are metallic, while the remainder are semiconducting:[8]

$$C_{Q,total} = \frac{1}{3}C_m + \frac{2}{3}C_{semi} \quad [13]$$

Calculation of double layer capacitance.

Before proceeding, we first note that the impact of CNT curvature on the double layer capacitance of an ionic liquid is expected to be small due to the short Debye length of ionic liquids. The Debye length λ_D is:

$$\lambda_D = \frac{1}{\sqrt{\frac{4\pi e^2 c^*}{\epsilon kT}}} = 1.7 \cdot 10^{-11}\ m \quad [14]$$

where c^* is the molecular (free charge) concentration in units of molecules per volume, e is the fundamental charge constant, and $\epsilon = 12.0 \pm 0.4$ is the static dielectric constant of EMIM TFSI.[9] The molecular concentration $c^* = 2\rho N_A / M_{IL}$, where $\rho = 1.52\ g/cm^3$ is the mass density for EMIM TFSI, N_A is Avogadro's number, and $M_{IL} = 391.31$ g/mol is the molar mass. This calculation yields a Debye length of 0.0170 nm (17 picometers). We can account for the impact of short-range ion correlations, by dividing the calculated Debye length by the parameter $\alpha = 0.112$ from Ref 10, yielding an effective Debye length of 0.050 nm. Considering a concentric cylindrical capacitor represented by a CNT with an effective capacitor plate spacing equal to the Debye length, we get the following expression for capacitance:

$$\frac{C_{dl}}{L} = \frac{2\pi k\epsilon}{\ln\left(\frac{R_{CNT} + \lambda_D}{R_{CNT}}\right)} \quad [15]$$

What this expression tells us is that when the CNT radius is significantly larger than the Debye capacitance, the capacitance approaches that of a planar electrode. This is the present case.

Nonetheless, we calculated the double layer capacitance as a function of CNT diameter and electrochemical potential by applying Goodwin and Kornyshev's (G-K) phenomenological model of ionic liquids to the geometric case of a cylindrical electrode.[10] Material parameters for EMIM TFSI were adapted from a report by Klein et al. (see Table S1).[11] Our analysis follows that in Ref 10, deviating in two important ways: 1) we do not make the assumptions necessary to generate a

closed-form solution for the capacitance; 2) we solve Poisson's equation in cylindrical coordinates rather than Cartesian coordinates.

Table S1. Material parameters of EMIM TFSI from Ref 11.

Parameter	Value
α	0.112
γ_+	0.260
γ_-	0.087
C_{PZC} $(\mu F\ cm^{-2})$	12.8
electrode mat'l	GC
method	EIS

We begin with the following definitions and assumptions:

- $x_+ \geq 0$ and $x_- \geq 0$ are the mole fractions of cation and anion of the ionic liquid, where $x_+ + x_- < 1$ since the lattice gas model assumes not all of the lattice sites are occupied.

- $u \in \boldsymbol{R}$ is a dimensionless electric potential, $u = \frac{e\phi}{k_B T}$

- $a_+, a_-, b \in \boldsymbol{R}$ are material parameters that characterize pair-wise interactions between cations (a_+), anions (a_-), and ion pairs (b)

- $0 \leq \gamma \leq 1$ is the so-called compacity parameter that represents the ratio of the average number of ions in the bulk to the number of ions in the densified double layer

Using equations 4 and 5 from Ref 10, we can express the potential u as a function of the relative distribution of ions:

$$a_+(\gamma/2 - x_+) + b(\gamma/2 - x_-) - \ln\left\{\frac{x_+}{1 - x_- - x_+}\frac{1-\gamma}{\gamma/2}\right\} = u \quad [16a]$$

$$a_-(\gamma/2 - x_-) + b(\gamma/2 - x_+) - \ln\left\{\frac{x_-}{1 - x_- - x_+}\frac{1-\gamma}{\gamma/2}\right\} = -u \quad [16b]$$

At a particular potential u, we can determine the mole fractions x_+ and x_- by numerically solving this pair of equations. In the symmetric case where anion and cation interaction terms are equivalent ($a_+ = a_- = a$) there is a closed-form analytical solution to the above system of equations:

$$x_+ = \frac{1}{2}\frac{\gamma \exp(-\alpha u)}{1 - \gamma + \gamma \cosh(\alpha u)} \quad [17a]$$

$$x_- = \frac{1}{2}\frac{\gamma \exp(\alpha u)}{1 - \gamma + \gamma \cosh(\alpha u)} \quad [17b]$$

where

$$\alpha = \frac{1}{1 + \frac{\gamma}{2}(a - b)} \quad [18]$$

We can re-introduce asymmetry (for example, due to steric differences in the cation and anion) through a potential-dependent $\gamma(u)$:

$$\gamma(u) = \gamma_- + \frac{\gamma_+ - \gamma_-}{1 + \exp(\alpha u)} \quad [19]$$

This logistic function yields a compacity parameter that tends asymptotically towards anion and cation compacity values (for positive and negative potentials, respectively).

For a cylindrical CNT with a potential distribution which only varies along *r*, we can write the 1-D Poisson equation in cylindrical coordinates:

$$\frac{1}{r}\frac{d}{dr}\left(r\frac{d}{dr}\,u\right)=\begin{Bmatrix}0, & r<r_{CNT}\\ \frac{x_+-x_-}{\gamma}, & r>r_{CNT}\end{Bmatrix} \quad [20]$$

Here, the radius is made unitless by dividing by the Debye length ($\lambda_D = 1.7\cdot 10^{-11}\ m$). The above expression can be re-written as:

$$\frac{d^2u}{dr^2}+\frac{1}{r}\frac{du}{dr}=\frac{x_+-x_-}{\gamma} \quad [21]$$

and $u(r)$ can be solved for numerically with the following boundary conditions:

- $\frac{du}{dr}\to 0$ as $r\to\infty$ (the potential flatlines far away from the CNT surface)
- $u(r=r_{CNT})=u_0$ (the potential at the CNT interface is fixed experimentally)

With a numerical solution for $u(r)$, we can determine the capacitance of the double layer by evaluating:

$$C_{dl}(u_0)=C_0\frac{d}{du_0}\left[\frac{du}{dr}\right]_{r=r_{CNT}} \quad [22]$$

In Figure S12 we show a comparison of the potential-dependent capacitance calculated using the above derivation in cylindrical coordinates, along with the analogous solution in Cartesian coordinates. Additionally, we include the results of the closed-form solution first presented in Ref 10:

$$C_{dl}=\pi\, d\, C_0\, \cosh(\alpha u/2)\frac{1}{1+2\gamma\sinh^2(\alpha\mu/2)}\sqrt{\frac{2\gamma\sinh^2(\alpha\mu/2)}{\ln(1+2\gamma\sinh^2(\alpha\mu/2))}} \quad [23]$$

All of the reported double layer capacitance values factor in the polydispersity of the CNTs by calculating the expectation value of C_{dl} over a normally-distributed population of CNT diameters:

$$\langle C_{dl} \rangle_d = \frac{1}{p} \sum C_{dl}(d) p(d) \qquad [24]$$

where $p(d)$ is a normally-distributed probability density centered at d_{avg} with a standard deviation of σ. Figure 4 in the main text uses double layer capacitance values from the full cylindrical model described above, including the effect of CNT polydispersity.

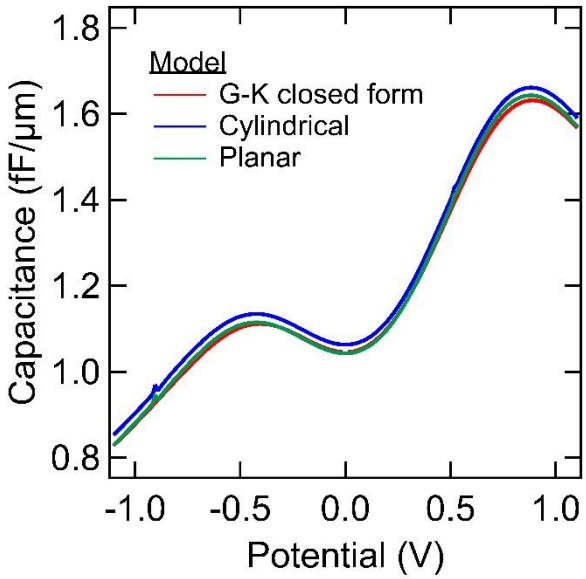

Figure S12. Impact of CNT curvature on the calculated differential capacitance. The Goodwin-Kornyshev (G-K) closed form solution is Equation 23. The cylindrical and planar traces are from our numerical evaluations of Poisson's equation in cylindrical and Cartesian coordinates, respectively. All traces incorporate the effect of CNT polydispersity. The potential here refers the potential drop between the electrode surface and the bulk ionic liquid.

Calculation of Fermi energy as a function of working electrode potential.

Having calculated C_Q and C_{dl}, we can now solve [1] and [2] to determine the Fermi energy for a particular working electrode potential. Combining [1] and [2]:

$$V_{WE} = \mu_F \left(\frac{C_Q + C_{dl}}{C_{dl}} \right) + V_{hf} \qquad [15]$$

Since C_{dl} and C_Q depend on V_{WE}, we evaluate this expression numerically and generate a closely-spaced series of values that relate V_{WE} to μ_F, the Fermi level of the CNTs. Looking at [15], in the limiting case where $C_{dl} \gg C_Q$ the entire potential V_{WE} is dropped across the CNTs. In other words,

μ_F shifts by the $|V_{WE}|$. In the opposite case ($C_{dl} \ll C_Q$), μ_F is static and the entire potential is dropped across the double layer. The results of this calculation are used in the main text to relate the applied electrochemical potential V_{WE} with the internal Fermi level $E_F = q\mu_F$ of the CNTs, where q is the fundamental charge constant (-e for electrons and +e for holes).

Supporting Information References

[1] Jiang, Z. GIXSGUI: a MATLAB toolbox for grazing-incidence X-ray scattering data visualization and reduction, and indexing of buried three-dimensional periodic nanostructured films. *Journal of Applied Crystallography* **2015**, *48* (3), 917-926.

[2] Meshot, E. R.; Park, S. J.; Buchsbaum, S. F.; Jue, M. L.; Kuykendall, T. R.; Schaible, E.; Bayu Aji, L. B.; Kucheyev, S. O.; Wu, K. J. J.; Fornasiero, F. High-yield growth kinetics and spatial mapping of single-walled carbon nanotube forests at wafer scale. *Carbon* **2020**, *159*, 236-246.

[3] Bengio, D.; Mendes, E.; Pellet-Rostaing, S.; Moisy, P. Electrochemical behavior of platinum and gold electrodes in the aprotic ionic liquid N,N-Trimethylbutylammonium Bis(trifluoromethanesulfonyl)imide. *Journal of Electroanalytical Chemistry* **2018**, *823*, 445-454.

[4] Ilani, S.; Donev, L. A. K.; Kindermann, M.; McEuen, P. L. Measurement of the quantum capacitance of interacting electrons in carbon nanotubes. *Nature Physics* **2006**, *2* (10), 687-691.

[5] Liang, J.; Akinwande, D.; Wong, H. S. P. Carrier density and quantum capacitance for semiconducting carbon nanotubes. *Journal of Applied Physics* **2008**, *104* (6), 064515.

[6] Li, J.; Pham, P. H. Q.; Zhou, W.; Pham, T. D.; Burke, P. J. Carbon-Nanotube–Electrolyte Interface: Quantum and Electric Double Layer Capacitance. *ACS Nano* **2018**, *12* (10), 9763-9774.

[7] Mintmire, J. W.; White, C. T. Universal Density of States for Carbon Nanotubes. *Physical Review Letters* **1998**, *81* (12), 2506-2509.

[8] Dresselhaus, G.; Dresselhaus, M. S.; Saito, R. *Physical Properties Of Carbon Nanotubes*; World Scientific Publishing Company, 1998.

[9] Huang, M.-M.; Jiang, Y.; Sasisanker, P.; Driver, G. W.; Weingärtner, H. Static Relative Dielectric Permittivities of Ionic Liquids at 25 °C. *Journal of Chemical & Engineering Data* **2011**, *56* (4), 1494-1499.

[10] Goodwin, Z. A. H.; Feng, G.; Kornyshev, A. A. Mean-Field Theory of Electrical Double Layer In Ionic Liquids with Account of Short-Range Correlations. *Electrochimica Acta* **2017**, *225*, 190-197.

[11] Klein, J. M.; Panichi, E.; Gurkan, B. Potential dependent capacitance of [EMIM][TFSI], [N1114][TFSI] and [PYR13][TFSI] ionic liquids on glassy carbon. *Physical Chemistry Chemical Physics* **2019**, *21* (7), 3712-3720.